ADVANCED MATERIALS
www.advmat.de

Impact of Ti and Zn Dual-Substitution in P2 Type $Na_{2/3}Ni_{1/3}Mn_{2/3}O_2$ on Ni–Mn and Na-Vacancy Ordering and Electrochemical Properties

Kei Kubota, Takuya Asari, and Shinichi Komaba**

High-entropy layered oxide materials containing various metals that exhibit smooth voltage curves and excellent electrochemical performances have attracted attention in the development of positive electrode materials for sodium-ion batteries. However, a smooth voltage curve can be obtained by suppression of the Na^+-vacancy ordering, and therefore, transition metal slabs do not need to be more multi-element than necessary. Here, the Na^+-vacancy ordering is found to be disturbed by dual substitution of Ti^{IV} for Mn^{IV} and Zn^{II} for Ni^{II} in P2-$Na_{2/3}[Ni_{1/3}Mn_{2/3}]O_2$. Dual-substituted $Na_{2/3}[Ni_{1/4}Mn_{1/2}Ti_{1/6}Zn_{1/12}]O_2$ demonstrates almost non-step voltage curves with a reversible capacity of 114 mAh g^{-1} and less structural changes with a high crystalline structure maintained during charging and discharging. Synchrotron X-ray, neutron, and electron diffraction measurements reveal that dual-substitution with Ti^{IV} and Zn^{II} uniquely promotes in-plane Ni^{II}–Mn^{IV} ordering, which is quite different from the disordered mixing in conventional multiple metal substitution.

1. Introduction

Na-ion batteries have recently attracted much attention for battery researchers[1–3] since acceptable cycle stability was achieved by hard carbon||O3 type $Na[Ni_{1/2}Mn_{1/2}]O_2$ full cell in 2009.[4] Owing to the rapid and significant developments of carbonous electrode materials, the negative electrode have recently achieved an extremely large reversible capacity of ≈480 mAh g^{-1}.[5] Therefore, to realize environmental-friendly and low-cost Na-ion batteries, development of higher energy positive electrode materials are of significant importance to increase the energy density of Na-ion cells and decrease the usage of expensive separators and non-aqueous electrolytes.[3]

Among sodium layered oxides, P2 type $Na_{2/3}[Ni_{1/3}Mn_{2/3}]O_2$ has a unique $\sqrt{3}\times\sqrt{3}$ superlattice structure with an in-plane Ni^{II}–Mn^{IV} honeycomb ordering and high water-stability[6] enabling facile handling in the battery assembly process. Electrochemical Na intercalation performance is also unique, almost all Na^+ ions can be extracted by charging to 4.5 V versus Na and reversibly intercalated into the structure by discharging. P2 type $Na_{2/3}[Ni_{1/3}Mn_{2/3}]O_2$ delivers a high reversible capacity of ≈150 mAh g^{-1} with a high discharge-voltage during a few cycles. However, the large reversible capacity rapidly deteriorates charge–discharge cycling.[7,8] The severe capacity decay is thought to be due to severe volume change in the phase transition from P2 $Na_x[Ni_{1/3}Mn_{2/3}]O_2$ to O2 type $[Ni_{1/3}Mn_{2/3}]O_2$ on charging to above 4.1 V,[8,9] and many researchers have devoted much effort on the improvement mainly using metal substitution.[9–14]

For the metal substitution, our group has emphasized the general trend that suitable valence state of metals and metal ratio exist in layered composite oxides like M^{II} and M^{IV} in $Na_{2/3}[M^{II}_{1/3}M^{IV}_{2/3}]O_2$ (M^{II} = Mg, Ni, Zn, Cu, M^{IV} = Mn, Ti, Sn).[15] As we earlier reported in 2014, partial Ti^{IV} substitution for Mn^{IV} in $Na_{2/3}[Ni_{1/3}Mn_{2/3}]O_2$ successfully suppresses the drastic volume change during charging of $Na_x[Ni_{1/3}Mn_{2/3}]O_2$ and improves cycle stability. Furthermore, the Ti substitution changes shape of voltage curves from stepwise into sloping and also increases average operating voltage.[9] The decrease in the number of voltage steps is known to originate from the suppression of Na^+-vacancy ordering and the decrease in the number of phase transitions during charge–discharge. This is caused by doped redox-inactive metals such as Ti^{IV}, whose Fermi level in the oxide is different from that of redox-active metals.[16,17] The Na^+-vacancy ordering is known to be governed by the complex interaction between Na^+ and Na^+ repulsion, Na^+ and TM^+ interaction, and TM charge ordering (TM = transition metals),[18] and evidenced by X-ray diffraction (XRD) and neutron diffraction (ND) measurements.[19–23] Indeed, the multi-elementalization

K. Kubota, T. Asari, S. Komaba
Department of Applied Chemistry
Tokyo University of Science
1–3 Kagurazaka, Shinjuku-ku, Tokyo 162-8601, Japan
E-mail: kubota.kei@nims.go.jp; komaba@rs.kagu.tus.ac.jp
K. Kubota
Research Center for Energy and Environmental Materials (GREEN)
National Institute for Materials Science (NIMS)
1-1 Namiki, Tsukuba, Ibaraki 305-0044, Japan

The ORCID identification number(s) for the author(s) of this article can be found under https://doi.org/10.1002/adma.202300714

DOI: 10.1002/adma.202300714

and disordering of metals in the slabs leads to a sloping voltage curve and excellent electrochemical properties. High-entropy materials containing various metals[24–26] such as $NaNi_{0.12}Cu_{0.12}Mg_{0.12}Fe_{0.15}Co_{0.15}Mn_{0.1}Ti_{0.1}Sn_{0.1}Sb_{0.04}O_2$[24] have attracted attention in the recent development of positive electrode materials for Na-ion batteries. Although multi-elementalization of the metals should not be necessary in terms of suppressing Na^+-vacancy ordering, the relationship between the Na^+-vacancy ordering and the atomic arrangement of 3d transiton metals with the dopted multi-element is not fully understood because 3d transition metals cannot be distinguished by XRD.

To fully understand the effect of multi-elements substitution, in this study, Mn^{IV} and Ni^{II} in P2 type $Na_{2/3}[Ni_{1/3}Mn_{2/3}]O_2$ were co-substituted with Ti^{IV} and Me^{II} (Me^{II} = Mg, Zn, Cu), respectively, and the correlation between their crystal structures (including Ni–Mn and Na^+-vacancy ordering) and electrochemical properties were investigated. Novel Ti^{IV} and Zn^{II} dual-substituted $Na_{2/3}[Ni_{1/3}Mn_{2/3}]O_2$ has demonstrated non-stepwise charge–discharge curves and delivering a reversible capacity of 114 mAh g^{-1} and high voltage of 3.60 V with excellent cycle stability. XRD, ND, and electron diffraction (ED) measurements were used to determine the effect of Ti^{IV} and Zn^{II} dual-substitution on Ni^{II}–Mn^{IV} ordering and Na^+-vacancy ordering. Furthermore, operando XRD and transmission electron microscopy (TEM) observation were carried out to elucidate highly stable crystalline structures of Ti^{IV} and Zn^{II} dual-substituted $Na_{2/3}[Ni_{1/3}Mn_{2/3}]O_2$.

2. Results and Discussion

2.1. $Na_{2/3}[Ni_{1/4}Mn_{1/2}Me_{1/12}Ti_{1/6}]O_2$ (Me = Mg, Cu, Zn)

2.1.1. Structural Characterization

$Na_{2/3}[Ni_{1/3-x}Mn_{1/2}Me_xTi_{1/6}]O_2$ (Me = Mg, Cu, and Zn, $x = 0$ and 1/12) were prepared by a solid-state reaction of Na_2CO_3 and metal oxides (see the details in the experimental section). The synthesized samples of $Na_{2/3}[Ni_{1/3}Mn_{2/3}]O_2$, $Na_{2/3}[Ni_{1/3}Mn_{1/2}Ti_{1/6}]O_2$, $Na_{2/3}[Ni_{1/4}Mn_{1/2}Ti_{1/6}Cu_{1/12}]O_2$, $Na_{2/3}[Ni_{1/4}Mn_{1/2}Ti_{1/6}Mg_{1/12}]O_2$, and $Na_{2/3}[Ni_{1/4}Mn_{1/2}Ti_{1/6}Zn_{1/12}]O_2$ are, hereinafter, referred to as "Non-sub", "Ti-sub", "Ti-Cu-sub", "Ti-Mg-sub", and "Ti-Zn-sub", respectively. Crystal structures of the synthesized Ti-substituted samples were identified by synchrotron XRD measurements. **Figure 1**a displays synchrotron powder XRD patterns of as-prepared Ti-sub, Ti-Mg-sub, Ti-Cu-sub, and Ti-Zn-sub samples. Observed Bragg diffraction peaks can be mainly indexed as an P2 type layered phase with a space group of $P6_3/mmc$, which is isostructural to $RbScO_2$.[27] Only in the case of Ti-Zn-sub sample, an impurity phase is detected and diffraction peaks at 34.4° and 36.3° in diffraction angles of 2θ are assigned to ZnO (ICSD#26170).[28] Even when the targeted Zn content x was reduced from 1/12 to 1/24 in $Na_{2/3}[Ni_{1/3-x}Mn_{1/2}Zn_xTi_{1/6}]O_2$, the diffraction peaks of ZnO are still detected as an impurity phase (see Figure S1 in the Supporting Information), indicating that the amount of Zn in the layered oxide (i.e., solid solution limit of Zn) is very small.

The superlattice peaks indexed as 1/6 2/3 l reflections are quite weak but are observed in the diffraction angle region of 2θ = 8–10° (Figure 1b). These superlattice peaks are mainly attributed

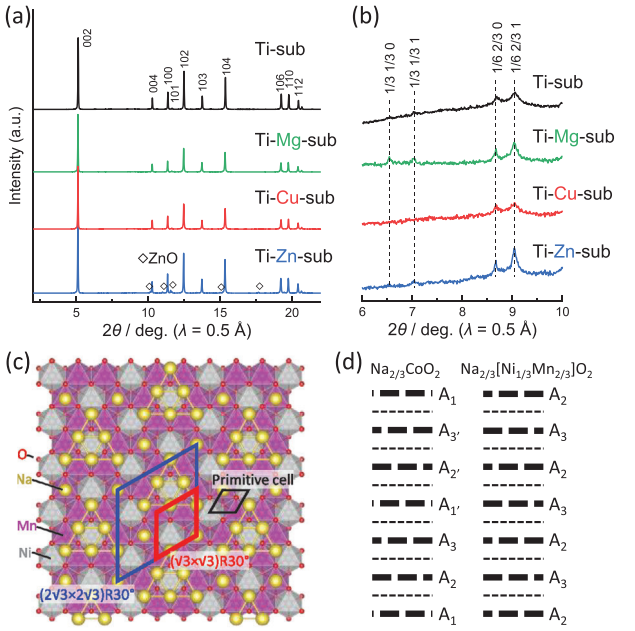

Figure 1. a) Synchrotron powder XRD patterns of as-prepared $Na_{2/3}[Ni_{1/3}Mn_{1/3}Ti_{1/6}]O_2$ (Ti-sub), $Na_{2/3}[Ni_{1/4}Mn_{1/2}Ti_{1/6}Mg_{1/12}]O_2$ (Ti-Mg-sub), $Na_{2/3}[Ni_{1/4}Mn_{1/2}Ti_{1/6}Cu_{1/12}]O_2$ (Ti-Cu-sub), and $Na_{2/3}[Ni_{1/4}Mn_{1/2}Ti_{1/6}Zn_{1/12}]O_2$ (Ti-Zn-sub) samples. b) Enlarged patterns of (a) in the diffraction angle range of 6.0–10.0°. c) Schematic of the in-plane Ni^{II}–Mn^{IV} and Na^+-vacancy ordering in P2-$Na_{2/3}[Ni_{1/3}Mn_{2/3}]O_2$, the same as reported by Lee et al.[8] and Gutierrez et al.[18] The primitive cell (black diamond) represents the conventional unit cell of typical P2 type materials such as P2-$Na_{2/3}[Co_{2/3}Mn_{1/3}]O_2$.[20] The hexagonal superstructure unit cell ($2\sqrt{3} \times 2\sqrt{3}$)R30° (blue diamond) has both Ni^{II}–Mn^{IV} and Na^+-vacancy ordering,[18] while the ($\sqrt{3}\times\sqrt{3}$)R30° superstructure unit cell (red diamond) has only Ni^{II}–Mn^{IV} ordering and cannot represent Na^+-vacancy ordering.[31] d) Schematic illustrations comparing stacking types of TMO_2 slabs in P2 type $Na_{2/3}TMO_2$. The thick dashed line represents the TMO_2 slab, and the thin dashed line represents the Na^+-vacancy layer.

to Na^+-vacancy ordering as reported for P2-$Na_{2/3}CoO_2$ and Non-sub,[8,17] while the superlattice peaks attributed to the in-plane TM ordering in the TMO_2 slab in 2θ = 6–8° are indexed as 1/3 1/3 l reflections. The latter superlattice peaks are visible in the XRD patterns only for light elemental substitution such as P2-$Na_{5/6}[Li_{1/4}Mn_{3/4}]O_2$[29] and P2-$Na_x[Mg,Mn]O_2$,[30] but are visible in the neutron diffraction patterns for almost any elemental substitution. The superlattice peaks of the Ni–Mn ordered ($\sqrt{3}\times\sqrt{3}$)R30° superstructure were reported with the neutron diffraction pattern by Lu et al.[6] Since the diffraction index h of the Na^+-vacancy ordered structure is half that of the Ni–Mn ordered one, a ($2\sqrt{3}\times2\sqrt{3}$)R30° superlattice is needed to represent Na^+-vacancy ordering in the Ni–Mn ordered structure as shown in Figure 1c.[18,31] Indeed, P2-$Na_{2/3}CoO_2$ has a specific in-plane Na^+-vacancy-ordering with a ($2\sqrt{3}\times2\sqrt{3}$)R30° superstructure (Figure S2a, Supporting Information) as almost the same proposed for Non-sub (Figure 1c).[20] However, the superlattice peaks in the XRD pattern of P2-$Na_{2/3}CoO_2$ are different from Non-sub and substituted samples (see Figure S2b, Supporting Information). One plausible reason for this is the difference in the

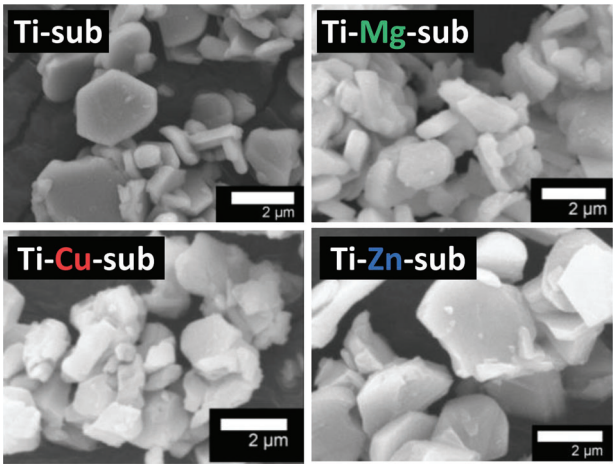

Figure 2. SEM images of as-prepared Ti-sub, Ti-Mg-sub, Ti-Cu-sub, and Ti-Zn-sub samples.

stacking structure of Na^+-vacancy layers, which correlates with the stacking sequence of TMO_2 slabs.

P2-$Na_{2/3}CoO_2$ has the stacking sequence of CoO_2 slabs, $A_1A_2A_3A_{1'}A_{2'}A_{3'}$ ($A_{1'}$ represents a slab of A_1 rotated 180° around $[1\bar{1}0]$) and a rhombohedral $2\sqrt{3}a \times 2\sqrt{3}b \times 3c$ cell with a space group of $R\bar{3}c$ (Figure 1d; Figure S2, Supporting Information).[20] On the other hand, in Non-sub, the stacking sequence of $[Ni_{1/3}Mn_{2/3}]O_2$ slabs was reported to be $A_2A_3A_2A_3$ with a hexagonal $\sqrt{3}a \times \sqrt{3}b \times c$ cell (Figure 1d) based on the ND results.[30,31] The detailed crystal structures of Non-sub and Ti-sub are discussed in detail in a later section based on the results of ND measurements. Here, a comparison based on XRD patterns suggests that Ti-Mg-sub and Ti-Zn-sub show similar peak profile of 1/6 2/3 *l* peaks, indicating similar Na^+-vacancy ordering and stacking. In contrast, Ti-Cu-sub and Ti-sub represent broader 1/6 2/3 *l* peaks, suggesting that Na^+-vacancy ordering is present with abundant stacking faults. Despite the differences in the peak profile of the superlattice peaks, all four Ti–Me-substituted samples exhibit similar morphology, hexagonal platelet particles a few microns in diameter as shown in **Figure 2**.

2.1.2. Electrochemical Properties

Electrochemical properties of the $Na_{2/3}[Ni_{1/3-x}Mn_{1/2}Me_xTi_{1/6}]O_2$ electrodes were examined in non-aqueous Na cells filled with 1.0 mol dm^{-3} $NaPF_6$/PC electrolyte. **Figure 3**a–d displays galvanostatic charge/discharge curves in the wide voltage range of 2.5-4.5 V at a current density of 13 mA g^{-1} for 40 cycles. Compared to Non-sub (160 mAh g^{-1} in Figure 3e), Ti-sub, Ti-Mg-sub, Ti-Cu-sub, and Ti-Zn-sub electrodes deliver smaller discharge capacities of 115–120 mAh g^{-1} at the initial cycle. Among them, the Ti-sub electrode exhibits pronounced stepwise voltage curves as observed in the case of Non-sub.[9] Such voltage steps are known to be caused by the ordering of sodium and vacancy in the interslab space and the simultaneous charge ordering (or dimerization or trimerization) of transition metal ions at the specific sodium content, such as $x = 2/3$, 1/2, and 1/3 in Na_xTMO_2.[8,32] In contrast, the dual-substituted samples with Ti and divalent metals represent smooth voltage curves. Distinct voltage-jump and -drop are seen only at the beginning and the end of charge and discharge. Although the initial charge–discharge profiles of the dual-substituted samples are similar, Ti-Cu-sub and Ti-Zn-sub electrodes demonstrate superior reversibility and excellent capacity retention for 40 cycles (Figure 3e). Despite the limited solubility of Zn in a solid-solution and its segregation as a ZnO particle, Zn-substitution is remarkably effective on smooth charge–discharge voltage profiles and improvent of cycle stability (see Figure S3, Supporting Information). Excellent capacity retention is achieved in the cases of Zn-rich Ti-Zn-sub samples ($x = 1/20$ and 1/12 in $Na_{2/3}[Ni_{1/3-x}Mn_{1/2}Zn_xTi_{1/6}]O_2$). When rate performance of Ti–Me-substituted samples is further compared (Figure 3f), Ti-sub and Ti-Mg-sub electrodes exhibit better rate-capability than Non-sub as previously reported.[14] Ti-Cu-sub and Ti-Zn-sub electrodes demonstrate further superior rate-performance and deliver more than 90% of the maximum reversible capacity at 2C-rate, which is much higher than Non-sub (33% retention). Furthermore, the Ti-Zn-sub electrode demonstrates high cycle-stability in the voltage ranges of 1.0–4.5 V and 2.5–4.8 V as well as 2.5–4.5 V (Figure S4, Supporting Information). The stability in the wider voltage ranges is much better than that of Non-sub reported previously.[8,9]

2.2. $Na_{2/3}[Ni_{1/3-x}Mn_{2/3-y}Zn_xTi_y]O_2$

2.2.1. Na^+-Vacancy Ordering and Ni–Mn Ordering

Focusing on Ti-Zn-sub, which demonstrated the best electrochemical performance among the Ti–Me-substituted samples, we will now discuss the effect of Ti-substitution and Ti–Zn dual-substitution. First, we compared ND patterns of $Na_{2/3}[Ni_{1/3}Mn_{2/3-y}Ti_y]O_2$ ($y = 0$, 1/6, 1/3, and 2/3) and Ti-Zn-sub in order to understand the Ni–Mn and Na^+-vacancy ordering as shown in **Figure 4**a. Similar to the previous report,[18,31] the ND pattern of Non-sub represents 1/3 1/3 *l* ($l = 0$, 1, 2, and 3) reflections in the *d*-spacing range of 2.7–4.5 Å, attributed to $\sqrt{3}\times\sqrt{3}$ superlattice with an in-plane honeycomb ordering of Ni–Mn in a slab and a stacking sequence of $A_2A_3A_2A_3$.[31] In addition to the 1/3 1/3 *l* reflections, 1/6 2/3 *l* ($l = 0$ and 1) reflections are also observed. The former 1/3 1/3 *l* superlattice peaks are quite weak and almost negligible in the synchrotron XRD pattern (Figure 4b), which is due to similar X-ray scattering factors but different neutron coherent scattering lengths of Ni and Mn (10.3(1) and −3.73(2) fm, respectively[33]). On the other hand, the latter superlattice peaks of 1/6 2/3 *l* reflections, observed in both XRD and ND patterns, are attributed to the in-plane Na^+-vacancy ordering with a $(2\sqrt{3}\times2\sqrt{3})$R30° superlattice.[8,18] Though the calculated structural model has been reported for Non-sub having both Na^+-vacancy and Ni–Mn ordering,[8] no structural model has been proved experimentally and a stacking sequence of Na^+-vacancy layers is not reported yet. Therefore, we considered both Na^+-vacancy and Ni–Mn orderings on the basis of calculated model which was predicted by DFT calculations and illustrated[8] as shown in Figure 1c. The crystal structure of Non-sub was modeled with a superstructure unit cell $2\sqrt{3}a \times 2\sqrt{3}b \times c$ and refined for the first time by the Rietveld method for the ND pattern of

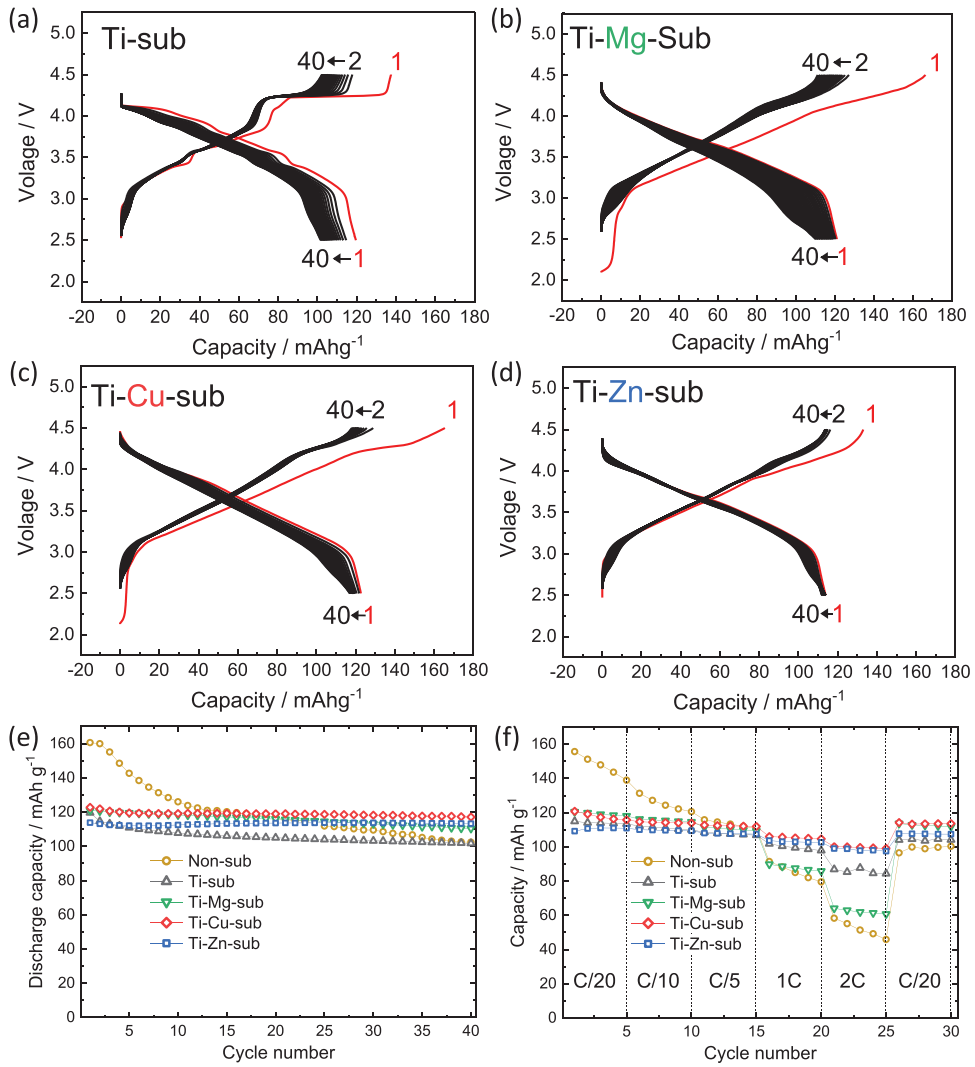

Figure 3. a–d) Galvanostatic charge–discharge curves of Ti-sub (a), Ti-Mg-sub (b), Ti-Cu-sub (c), Ti-Zn-sub (d) electrodes in non-aqueous Na cells. e) Cycle stability and f) rate performance of the electrodes.

Non-sub in the large *d*-spacing value region ($d \geq 4$) obtained by a low-angle bank detector.

The refinement results of the ND patterns (Figure S5, Supporting Information) and structural parameters (Table S1, Supporting Information) represent good agreement between the observed and calculated patterns. The refined structure with a space group of $P6_3$ has an in-plane Na^+-vacancy ordering as well as an in-plane Ni–Mn ordering in the slab with the slab stacking of $A_2A_3A_2A_3$ as shown in Figure 4c. The in-plane Na^+-vacancy ordering is identical to that of the theoretically predicted model[8] and that of P2-$Na_{2/3}CoO_2$.[20] Following the stacking sequence of Na^+-vacancy layers in P2-$Na_{2/3}CoO_2$ (Figure S2, Supporting Information), the overall stacking sequence in Non-sub is $A_3\alpha_1A_2\alpha_3A_3\alpha_1A_2\alpha_3$. Although the good refinement results are obtained for the ND pattern detected by a low-angle bank detector, the ND pattern detected by a high-resolution bank detector and the synchrotron XRD pattern show split 220, $22\bar{1}$, and $22\bar{3}$ reflections at a *d*-spacing of around 2.504, 2.443, and 2.077 Å, respectively, which is different from single peaks of the calculated pattern (Figure S6, Supporting Information). The fact suggests slightly different lattice parameters of *a* and *b*, and an orthorhombic or monoclinic lattice instead of the abovementioned hexagonal one. Due to the presence of stacking defects as indicated by broader 1/6 2/3 1 reflection than 1/6 2/3 0 reflection (Figure 4b), it was difficult to perform more precise structural refinements for the ND and XRD patterns.

Instead, the SAED pattern of Non-sub along the 001 zone axis proves clear differences in symmetry between *a*- and *b*-axes (Figure 4d). When the diffraction spots are indexed with the $2\sqrt{3}\times2\sqrt{3}$ superlattice model, *hk*0 (h, $k = \pm 2n$) spots such as 220 and $\bar{2}40$ reflections are remarkably bright and have six-fold rotational symmetry, typically observed for the P2-type (γ-type) Na_xCoO_2 ($P6_3/mmc$) phase with randomly occupied Na sites.[34] Between the bright spots, characteristic additional small spots are observed. For example, the spots of 200 and 400 reflections and those of 020 and 040 ones are observed along a^* and b^* axis,

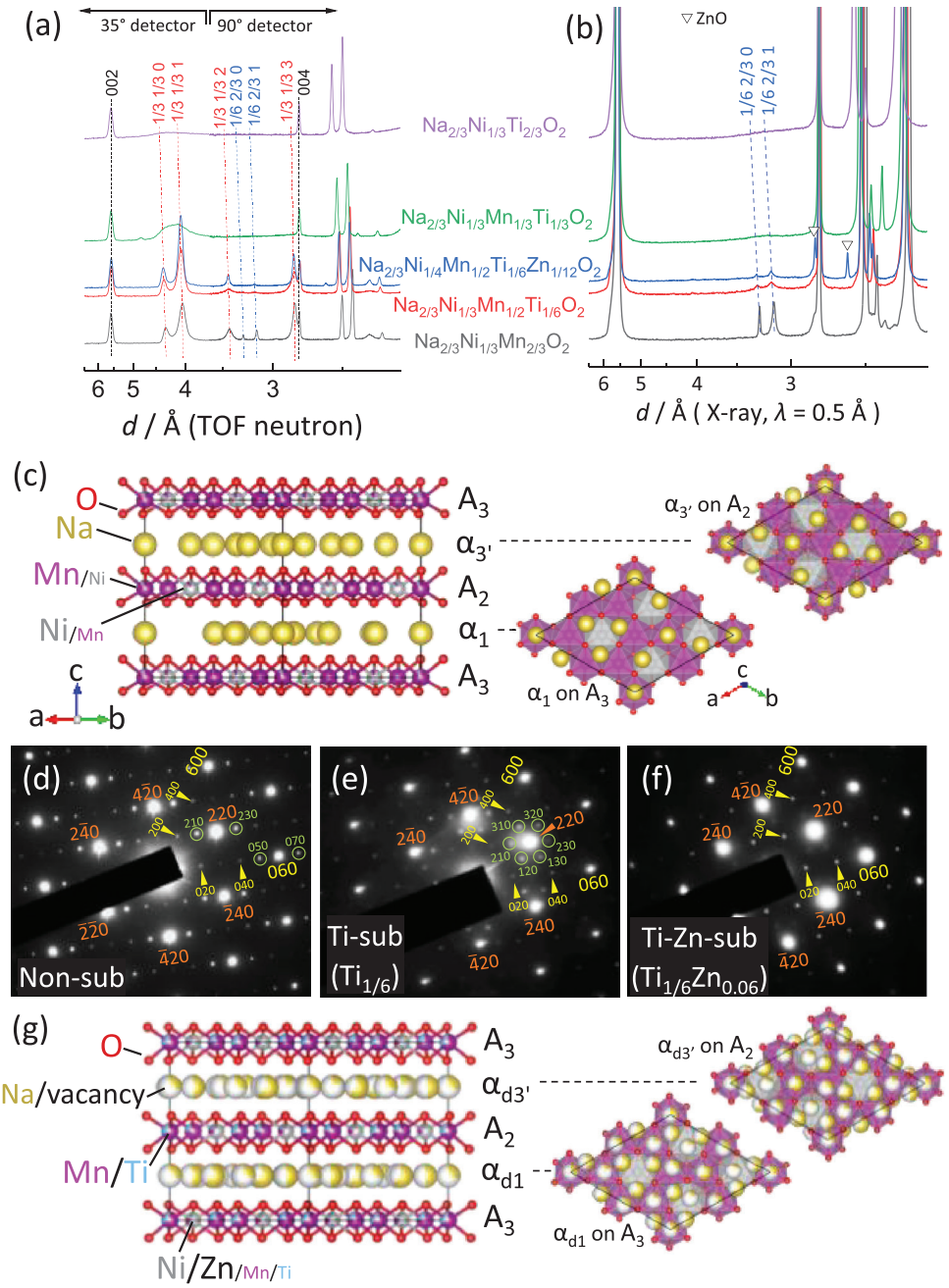

Figure 4. a) ND and b) XRD patterns of $Na_{2/3}[Ni_{1/3}Mn_{2/3}]O_2$ (Non-sub), $Na_{2/3}[Ni_{1/3}Mn_{1/3}Ti_{1/6}]O_2$ (Ti-sub), $Na_{2/3}[Ni_{1/3}Mn_{1/3}Ti_{1/3}]O_2$, and $Na_{2/3}[Ni_{1/4}Mn_{1/2}Ti_{1/6}Zn_{1/12}]O_2$ (Ti-Zn-sub) samples. c) Schematic illustrations of a refined hexagonal superlattice structure of Non-sub. d–f) Selected-area electron diffraction (SAED) patterns of Non-sub (d), Ti-sub (e), and Ti-Zn-sub (f) samples along the $[001]_{hex.}$ zone axis. g) Schematic illustrations of a refined hexagonal superlattice structure of Ti-Zn-sub. To compare the structures with that of P2-$Na_{2/3}CoO_2$ in Figure S2 (Supporting Information), the atomic positions in (c) and (g) were transformed and differ from the standardized structural parameters in Tables S2 and S3 (Supporting Information), respectively.

respectively. However, $h00$ ($h = \pm(6n \pm 1)$) reflection spots such as 100 and 500 are not seen along the a^* axis despite $0k0$ ($k = \pm(6n \pm 1)$) spots such as 050 and 070 are visible along b^* axis. This indicates that the symmetry elements of the a- and b-axes are different, and the lattice might not be hexagonal at room temperature. Even if the lattice is hexagonal, the $hk0$ ($h = \pm 2n$, $k = \pm(6n \pm 1)$) satellite spots such as the 050/070 and 210/230 reflections observed to the left and right around the bright $hk0$ (h, $k = \pm 2n$) spots cannot be indexed with a conventional Ni–Mn ordered $\sqrt{3}a \times \sqrt{3}b$ superlattice but can be indexed with a $2\sqrt{3}a \times 2\sqrt{3}b$ superlattice. The fact indicates the presence of Na^+-vacancy ordering with a pseudo $2\sqrt{3}a \times 2\sqrt{3}b$ superlattice in Non-sub.

When the ND and XRD patterns of Ti-substituted samples $Na_{2/3}[Ni_{1/3}Mn_{2/3-y}Ti_y]O_2$ (y = 1/6, 1/3, and 2/3) are compared with those of Non-sub in Figure 4a,b, the peak intensity of the 1/6 2/3 l (l = 0 and 1) reflections, which are attributed to the Na^+-vacancy ordering in the superstructure $2\sqrt{3}a \times 2\sqrt{3}b \times c$, decreases with increase in the Ti content. Simultaneously, the 1/3 1/3 l reflections also become weaker. In $Na_{2/3}[Ni_{1/3}Ti_{2/3}]O_2$ (y = 2/3), the absence of superlattice peaks is the same result reported by Paulsen,[30] suggesting the absence of Na^+-vacancy or Ni-Ti in-plane ordering. This is a similar trend for cobalt substitution for nickel in $Na_{2/3}[Ni_{1/3}Mn_{2/3}]O_2$, $Na_{2/3}[Ni_{1/3-x}Co_xMn_{2/3}]O_2$.[31] Consequently, substitution of Ti^{IV} having an intermediate ionic radius (0.605 Å at a octahedral site[35]) between Ni^{II} (0.69 Å) and Mn^{IV} (0.53 Å) simultaneously disturbs both Ni–Mn and Na^+-vacancy ordering. In the slightly Ti-substituted sample of Ti-sub (y = 1/6), the 1/6 2/3 l superlattice peaks are weak but certainly observed in the ND pattern (Figure 4a), but the 1/6 2/3 l peaks as well as 1/3 1/3 l ones are very broad, indicating the presence of stacking faults in the structure having Ni–Mn and Na^+-vacancy ordering. In the SAED pattern of Ti-sub (Figure 4e), six-fold rotating blurry satellite spots are observed surrounding the bright spot, which is obviously different from the satellite spots that are sharply visible only on the left and right sides of the bright spot in Non-sub. The high-resolution ND pattern of Ti-sub, indeed, shows single peaks of 220, $22\bar{1}$, and $22\bar{3}$ reflections and confirms a hexagonal symmetry (Figure S7, Supporting Information). Consequently, complete replacement of Mn^{IV} by Ti^{IV} is found to disrupt both Ni^{II}-Ti^{IV} and Na^+-vacancy ordering, and slight Ti-substitution has led to a hexagonal lattice symmetry with Na^+-vacancy ordering but with a high degree of stacking defects in the structure.

Finally, Ti–Zn dual-doping effect is discussed with comparing the ND, XRD, and SAED patterns of Non-sub, Ti-sub, and Ti-Zn-sub. As seen for the Ti-sub, the peak intensity of the 1/6 2/3 l superlattice peaks is quite lower for Ti-Zn-sub than Non-sub, proving a suppressed Na^+-vacancy ordering in Ti-Zn-sub. Differing from the Ti-sub, the 1/3 1/3 l superlattice peaks get rather stronger and sharper than Non-sub (Figure 4a), evidencing highly ordered structure including the Ni–Mn ordering and less stacking faults. These results suggest that the peak intensity of the 1/6 2/3 l reflection is weak in Ti-Zn-sub, which is almost the same as in the Ti-sub case, but the cause is quite different. Furthermore, in the SAED pattern of Ti-Zn-sub (Figure 4f), satellite spots surrounding the bright $hk0$ (h, $k = \pm 2n$) spots are quite weak, while small spots such as 200, 400, 020, and 040 reflections, corresponding to the $\sqrt{3}\times\sqrt{3}$ superlattice with a Ni–Mn ordering, are clearly observed. These are consistent with the results of ND and XRD. Moreover, single peaks of 220, $22\bar{1}$, and $22\bar{3}$ reflections are also confirmed in the ND pattern (Figure S7, Supporting Information) and can be indexed with a hexagonal unit cell. Since the diffraction peaks/spots of 1/6 2/3 l reflection are quite weak but certainly observed in Figure 4a,b,f, a $2\sqrt{3}a \times 2\sqrt{3}b \times c$ superstructure unit cell same as the case of Non-sub (Figure 4c) was used for Rietveld refinement of the synchrotron XRD and ND patterns (Figure S8, Supporting Information). We have succeeded in fitting the experimental data of XRD and ND with satisfactory reliability factors of the refinement as shown in Figure 4g and Table S2 (Supporting Information). The refined structure

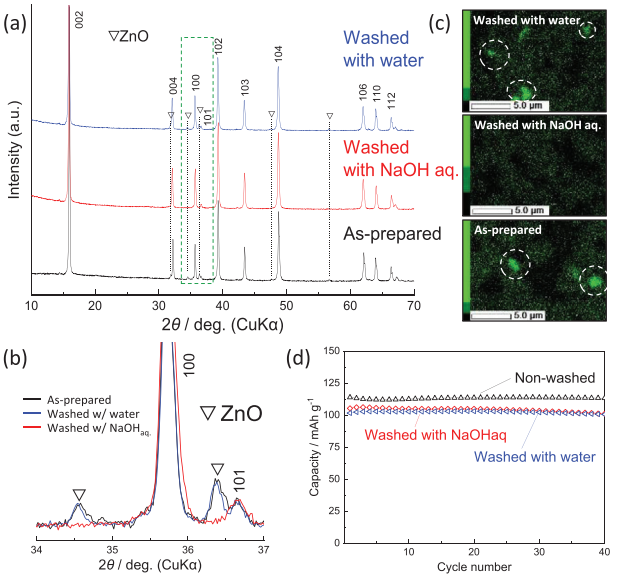

Figure 5. a) Whole and b) narrow angle ranges of XRD patterns, and c) SEM-EDS mapping of Zn element for the Ti-Zn-sub samples in the states as-synthesized, treated with distilled water, and treated with NaOH aqueous solution. d) Cycle stability of the electrodes of the untreated and treated Ti-Zn-sub samples.

uniquely proves the almost Na-disordered (widely and randomly Na-distributed) and Ni–Mn ordered $2\sqrt{3}a \times 2\sqrt{3}b \times c$ superlattice for Ti-Zn-sub. Although multi-element substitution is generally thought to result in a disordered arrangement of metals in a slab, dual-substitution with Ti^{IV} and Zn^{II} uniquely promotes Ni^{II}–Mn^{IV} ordering.

2.2.2. Water Stability and Effect of ZnO Impurity

Lu et al. pointed out high water-stability for in-plane Ni–Mn ordered materials,[6] although the water resistance mechanism applicable to all layered oxides is still debatable.[36] To test water stability of Ti-Zn-sub and any effect of the ZnO impurity phase on the electrochemical performance, ZnO particles were removed from the Ti-Zn-sub powder sample through treatment with aqueous sodium hydroxide solution because ZnO is generally known to be soluble in basic NaOH aqueous solution. We also prepared a sample that was treated with deionized water to check its stability in water.[37] **Figure 5**a,b displays the XRD patterns of the treated Ti-Zn-sub samples. Diffraction peaks of a crystalline ZnO phase are observed for the as-prepared and water-treated samples but completely disappear for the $NaOH_{aq.}$-treated sample. Energy-dispersive X-ray spectrometry (EDS) mappings for Zn also prove that ZnO particles are removed by treating with NaOH solution as shown in Figure 5c (see EDS mappings for other elements in Figure S9, Supporting Information). Inductively coupled plasma atomic emission spectrometry (ICP-AES) results reveal slight decrease of Zn amount in the solid-solution from 0.082 to 0.056 for the Ti-Zn-sub sample after the treatment with the NaOH aqueous solution as shown in Table S3 (Supporting Information). Even after treating with deionized water, the XRD peak intensity and peak position of the P2 type phase are almost the same as those

of the untreated Ti-Zn-sub sample, indicating the high stability of the Ti-Zn-sub sample in water. Although the reversible capacities of both treated samples are slightly lower, their cycle stability is comparable to that of the untreated sample, confirming no apparent effects of the impurity phase of ZnO as well as the aqueous wet process on the electrochemical performance as shown in Figure 5d and Figure S10 (Supporting Information).

From the above results and discussion, we found that Ti–Zn dual-substitution retains in-plane Ni–Mn ordering as well as water stability and suppresses Na^+-vacancy ordering as well as stacking faults. One can see the remarkable effect of suppressed Na^+-vacancy ordering in the sloping and smooth voltage curves compared to those of Ti-sub (Figure 3). The stepless curves indicate a least structural changes and phase transition during charging and discharging, which is expected to explain the longer cycle-life and higher rate performances. We further conduct operando XRD to elucidate exact phase transformation during charge–discharge processes.

2.2.3. Structural Evolution During Charge–Discharge

To understand the relationship between the voltage curves and structural evolution of the layered oxides, operando XRD was carried out for Non-sub, Ti-sub, and Ti-Zn-sub electrodes during 1st charge and discharge at a low current rate of C/50 as shown in **Figure 6** and Figures S11–S13 (Supporting Information). In the operando XRD patterns of Ti-sub (Figure S12, Supporting Information), there is a lack of data during charging, which is due to temporary trouble of the diffractometer and not due to the electrochemical test. As expected from the almost non-stepped charge–discharge curves of Ti-Zn-sub, the operando XRD patterns (Figure 6a; Figure S13, Supporting Information) show almost monotonous and continuous peak-shift of diffraction peaks. In contrast, as several voltage steps are seen in the charge–discharge curves (Figure S11a, Supporting Information), Non-sub electrode represents repetitive intensity-gain/-reduction of diffraction peaks in the operando XRD patterns (Figure S11b, Supporting Information) in the voltage regions below the high-voltage plateau located at 4.20 V on charging and at 4.06 V on discharging (Figure S11a, Supporting Information). These variation in diffraction intensity and peak position are not highly remarkable but the observed repetitive intensity-gain/-reduction indicates several two-phase reactions. A slight but repetitive increase/decrease in the intensity of the diffraction peaks is also observed for the Ti-sub electrode (Figure S12, Supporting Information), as expected from the observation of satellite spots attributed to Na^+-vacancy ordering in the SAED pattern (Figure 4e).

More distinct differences are found in the high voltage region above 4.0 V (Figure 6c–f). Non-sub electrode clearly exhibits disappearance of 002_{P2} reflection and simultaneous appearance of 002_{O2} reflection without a peak shift during charging in Figure 6c, suggesting a two-phasic reaction from P2 type to O2 type transition in the flat voltage region as reported in the literature.[7] Ti-sub electrode also shows disappearance of 002_{P2} on charging, but a simultaneously appeared peak is very broad and weak in intensity (Figure 6d). Furthermore, despite the flat voltage region at ≈4.25 V on the 1st charging (Figure S12a, Supporting Information), the newly appearing peak around $2\theta = 17°$ gradually shifts toward higher diffraction angle. The observed broad and weak peak indicates presence of multiple phases and/or lower periodicity of the slabs stacking including a high degree of stacking faults. On the contrary, Ti-Zn-sub electrode retains sharp diffraction peaks above 4.0 V (Figure 6e). Unlike Non-sub and Ti-sub, a new peak is observed around $2\theta = 16.2°$ between the two peaks at $2\theta = 15.7°$ and 17° (see the enlarged patterns in Figure S13c, Supporting Information). The fact indicates possible formation of an intermediate intergrowth between P2 and O2 types such as OP4 type[38–40] and a more coherent slab-stacking than Ti-sub.

When synchrotron XRD patterns of the fully charged electrodes are compared among the three samples as shown in Figure S14a (Supporting Information), the main phase of all the three samples is found to be O2 type phase. However, their lattice parameters are different, which is confirmed as different peak positions of 002 and 110 reflections in Figure S14b (Supporting Information). It should be noted that the broadening of the 10*l* reflections is due to the stacking faults of the TM slabs, because it is equally possible to form two different O2-type structures from a P2-type one by two different gliding vectors of the TM slabs.[39] Even in the synchrotron XRD pattern (Figure S14, Supporting Information), 002 peak of the Ti-sub electrode is much broader than the other two samples, which is consistent with the operando XRD patterns in Figure 6d. A minor phase having smaller *a* and *c* lattice parameters should co-exist in the charged Ti-sub electrode. When diffraction peaks are indexed with a conventional small hexagonal lattice, the lattice parameters of the samples charged to 4.5 V are calculated as $a = 2.845$ Å and $c = 8.877$ Å for Non-sub, $a = 2.83$ Å and $c = 10.1$ Å for Ti-sub, and $a = 2.862$ Å and $c = 10.768$ Å for Ti-Zn-sub. The interslab distance of the hexagonal O2 type phage for Non-sub, Ti-sub, and Ti-Zn-sub is 4.438, 5.05, and 5.384 Å, respectively. The Ti–Zn dual substitution successfully suppresses the interslab shrinkage.

From the above discussion, we schematically summarize structural change mechanism in Figure 6f. By Na extraction in Non-sub, O2 type domains are grown with disappearance of P2 type domains, resulting in the P2–O2 transition with distinct phase separation. In contrast, Ti-sub has a wider distribution of the TM slabs with different Na concentrations in the interslab space during charging above 4.0 V. The stacking defects induced by Ti substitution, which is confirmed with the ND and SAED patterns, would lead to random Na extraction, resulting in disturbing the phase separation between P2 and O2 types and/or destabilization of intermediate P–O phases. In the case of Ti–Zn dual-substitution, X-ray absorption near-edge structure (XANES) data represent reversible energy shift of only Ni K-edge during charging and discharging and no significant energy shift for Mn, Ti, and Zn K-edge (**Figure 7**). The fact suggests that nickel redox mainly participates in the redox reaction and Zn^{II} is not oxidized by charging and would attract sodium ions in the structure as an electrochemically inactive metal (Figure 7d). Furthermore, the Zn K-edge spectra, which show a reversible return to the initial state, indicate that Zn is not migrated, such as irreversible extraction on charging. The Ni K-edge energy of Ti-Zn-sub at 4.5 V is very close to that of the reference material, $LaNi^{III}O_3$. As recent papers reported for Non-sub with O K-edge XAS and resonant inelastic X-ray scattering (RIXS) spectra,[41–42] only the nickel redox cannot explain charging and discharge capacities. Lattice oxygen

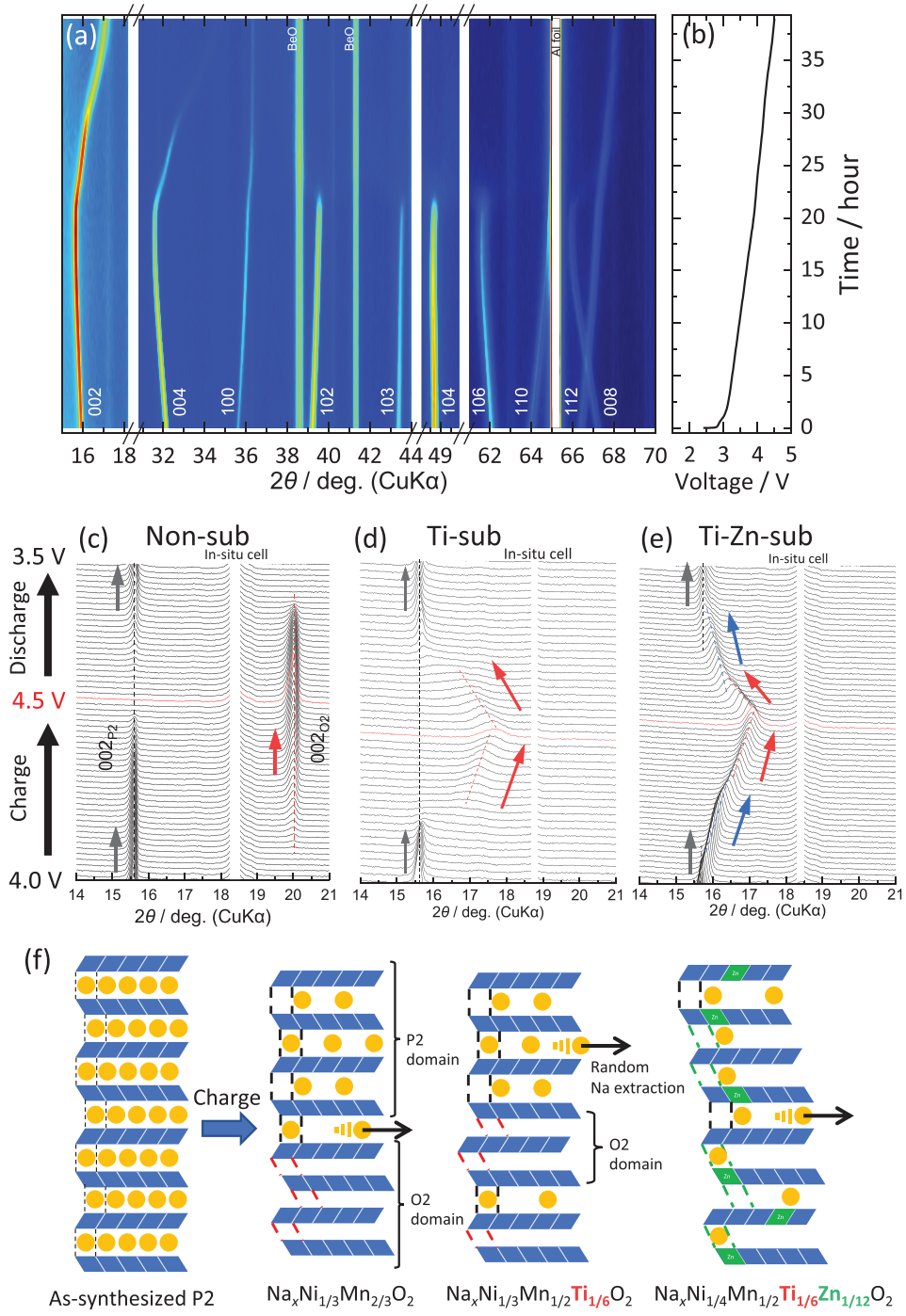

Figure 6. a) Contour plots of operando XRD patterns and b) simultaneously collected voltage curve of the Ti-Zn-sub electrode during the initial charging process. c–e) Selected operando XRD patterns of Non-sub (c), Ti-sub (d), and Ti-Zn-sub (e) electrodes. f) Schematic illustrations of structural change mechanism.

should take part in the charge compensation mechanism of Ti-Zn-sub during charging and discharging as an anion redox without oxygen gas generation. Thus, oxidation of nickel and oxide ions during charging results in reducing the averaged Na concentration in the interslab space, changing the structures from a widely spaced P2-type structure to a narrowly spaced O2-type one. Nevertheless, the O type layer in the O2 type phase of Ti-Zn-sub has wider interslab space than the other two samples. Formation of the wider interslab space of the O type layer would facilitate faster P2–O2 transition in Ti-Zn-sub with keeping the high crystallinity along the stacking direction. Furthermore, the presence of the P2–O2 intermediate phase observed in Figure 6e would

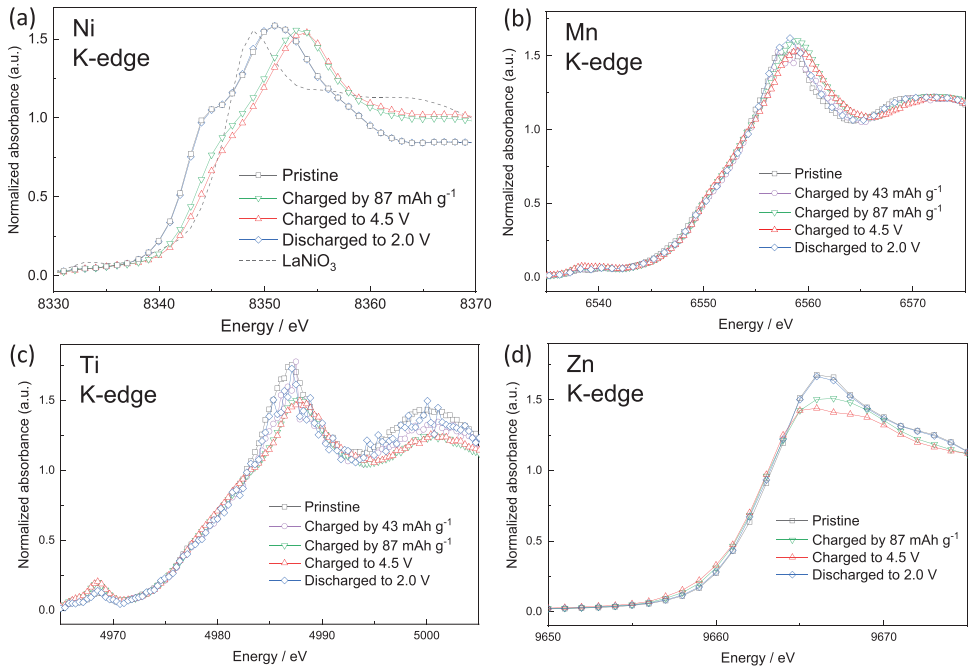

Figure 7. a–d) Ex situ XANES spectra of the Ti-Zn-sub electrodes at Ni K-edge (a), Mn K-edge (b), Ti K-edge (c), and Zn K-edge (d). The Ni K-edge spectrum of $LaNiO_3$ as a standard reference is shown in (a).

compensate for the small but present lattice mismatch between the P2 and O2 phases.

Large repetitive changes in interslab distance (or volume) during charging and discharging are known to cause cracks in the particles, resulting in capacity degradation during cycling, as reported for Non-sub with a 23% shrinkage in volume.[43] Based on the synchrotron XRD results (Figure S14, Supporting Information), shrinkage ratio in volume between the pristine and fully charged states is 13% for Ti-sub and 7% for Ti-Zn-sub. The suppressed volume shrinkage can explain the better cycle stability and rate capability for Ti-sub and Ti-Zn-sub samples.

2.2.4. Particle Surface Morphology after Cycling

To confirm the metal-substitution effect on the particle surface after cycling, ex situ TEM observation was performed for the Non-sub, Ti-sub, and Ti-Zn-sub electrodes after 10 cycles (**Figure 8**). Although large cracks breaking particles are not observed after 10 cycles, corrosive pits with 15–20 nm in depth are seen at the outermost surface of Non-sub particles as previously reported.[44] Ti-sub also shows corrosive pits at the outermost surface, but the pits are fewer and shallower (≈10 nm) than those of Non-sub. Surprisingly, no corrosive pits are observed for Ti-Zn-sub particles, indicating the stable particle surface during cycling. Similar to the case of P2-$Na_{2/3}[Al_{1/18}Ni_{11/36}Mn_{23/36}]O_2$,[15] the stable surface would result in the excellent performance of Ti-Zn-sub.

The Ti–Zn dual-substituted layered oxide retains the original wide interslab space during charging, contributing to suppression of the structural stress between the P2 and O2 phases and stabilization of the crystal structures in both bulk and surface. In the present study, high concentration of Ti or Zn was not

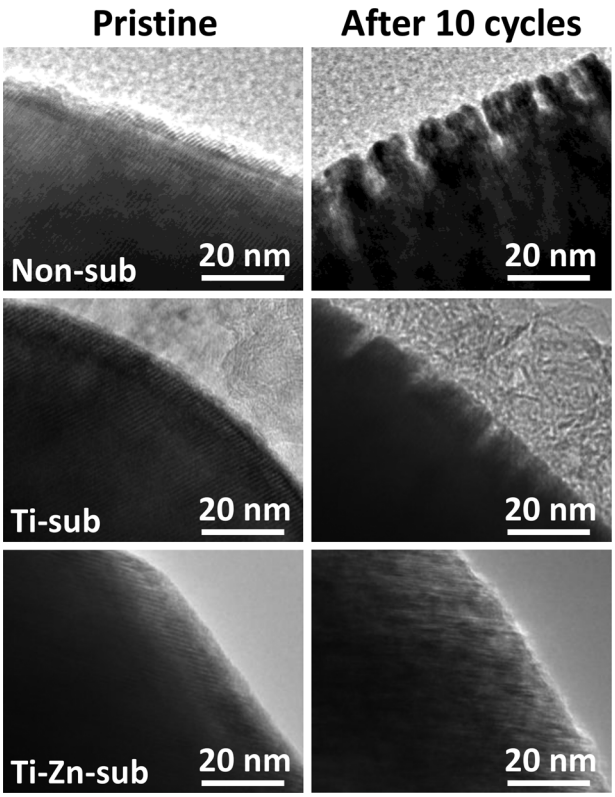

Figure 8. TEM images of the Non-sub, Ti-sub, and Ti-Zn-sub electrode samples in the pristine (left) and 10 cycled (right) states.

found on the outermost surface, but doped Ti possibly protect the particle surface against HF attack during electrolyte decomposition at high voltage as reported for $NaMn_{0.8}Ti_{0.1}Ni_{0.1}O_2$.[45] In the present Ti-Zn-sub sample, the excess Zn is not present as a thin ZnO coating layer with a few nanometers in thickness,[46] and is contained as ZnO particles of several hundred nanometers. Further optimizing of synthesis conditions such as Zn content, starting materials, precursors, and calcination temperature and time would reduce electrochemically inactive and insulating ZnO particles and the optimal P2-Na_x[Ni, Mn, Ti, Zn]O_2 is expected to demonstrate further improved electrochemical properties. Furthermore, we hope that the findings of this study will lead to the understanding that conventional metal substitution, which is a disorderly mixing of metals in a slab, is not always the best method, and that the further development of metal substitution methods yield promising positive electrode materials for Na-ion batteries.

3. Conclusion

In $Na_{2/3}[Ni_{1/3-x}Mn_{2/3-y}Me_xTi_y]O_2$ (Me = Mg, Cu, Zn), the effects of substitution by titanium and divalent metals of Mg, Cu, and Zn on the crystal structure and electrochemical properties have been studied. The Ti–Zn and Ti-Cu dual-substituted samples demonstrate superior cycle stability and rate capability in non-aqueous Na cells in the voltage range of 2.5–4.5 V. The novel moisture-stable positive electrode material of $Na_{2/3}Ni_{1/4}Mn_{1/2}Ti_{1/6}Zn_{1/12}O_2$ exhibits non-stepwise charge–discharge voltage curves and delivers a reversible capacity of 114 mAh g^{-1} with an average discharge voltage of 3.60 V versus Na. Comparing the three samples of non-substituted, Ti-substituted, and Ti–Zn dual-substituted samples, synchrotron X-ray, neutron, and electron diffraction measurements reveal modified Ni–Mn and Na^+-vacancy orderings by the substitution. Dual-substitution by Ti^{IV} and Zn^{II} maintains the Ni^{II}–Mn^{IV} ordering but disrupts the Na^+-vacancy ordering, leading to the smooth voltage curves with less structural changes. The amount of solid-solution Zn is very small (≈0.06 per formula unit), but dual-substituting with Ti and Zn uniquely promotes Ni^{II}–Mn^{IV} ordering and improves electrochemical sodium (de)intercalation properties.

4. Experimental Section

Synthesis Procedures: $Na_{2/3}[Ni_{1/3-x}Mn_{2/3-y}Me_xTi_y]O_2$ (Me = Mg, Cu, and Zn, $x = 1/12$ for the Mg and Cu cases and $x = 0$, 1/24, 1/20, and 1/12 for the Zn case, $y = 1/6$) and $Na_{2/3}[Ni_{1/3}Mn_{2/3-y}Ti_y]O_2$ ($y = 0$, 1/6, 1/3, and 2/3) were prepared by a solid-state reaction. Reagent grade Na_2CO_3 (Nacalai Tesque, Inc., 99.8%), and NiO (FUJIFILM Wako Pure Chemical Corporation), TiO_2 (anatase, Sigma-Aldrich Co. LLC), MgO (Kishida Chem. Co., Ltd.), Cu_2O (Kishida Chem. Co., Ltd.), ZnO (Kanto Chemical Co., Ltd.) and Mn_2O_3 prepared by calcining $MnCO_3$ (Kishida Chem. Co., Ltd., 44% as Mn content) at 700 °C were used as starting materials. 5 mol% excess amounts of Na_2CO_3 were added in starting materials in the consideration for the high volatility of sodium oxides during the heat treatment. The starting materials were ball-milled with acetone at 600 rpm for 12 h by using a planetary ball mill (PULVERISETTE 7 classic line, Fritsch Japan Co., Ltd). The mixture was dried and pelletized, then heated to 900 °C in air at a temperature increase rate of 5 °C min^{-1}, and the temperature was held for 12 h. After the calcination, the samples were taken out from the furnace without cooling process, and then immediately transferred into an argon-filled glove box. The samples were cooled to room temperature in the glove box and were kept inside to avoid the exposure to moisture in air.

Structural and Morphological Characterization: Structures of the $Na_{2/3}[Ni_{1/3-x}Mn_{2/3-y}Me_xTi_y]O_2$ samples were identified by using an X-ray diffractometer (SmartLab, Rigaku Corporation) equipped with a high-speed position sensitive detector (D/teX Ultra, Rigaku Corporation) and Ni-filtered Cu Kα radiation as an X-ray source. The samples were fixed in a homemade air-tight sample holder during XRD measurements to avoid air exposure. Detailed structures of the samples were determined with a synchrotron X-ray diffractometer at BL02B2[47] of SPring-8 in Japan, equipped with a large Debye-Scherrer camera. For ex situ measurements, samples were electrochemically prepared in the coin type cells and sodium content was calculated from the charge passed. The composite electrodes, taken out from the coin cells, were rinsed with propylene carbonate (PC, Kishida Chemical Co., Ltd.) and then with diethyl carbonate (DEC, Kishida Chemical Co., Ltd.) to remove an electrolyte salt and then dried at room temperature in an Ar-filled glovebox. The oxide composites were separated from the aluminum current collectors, crushed into powders. As-prepared and electrochemically tested samples were put into glass capillaries with 0.3 and 0.5 mm in diameter, respectively. The glass capillaries were sealed with a resin in the glovebox or by heating and melting the end of glass capillaries to eliminate sample exposure to air. To minimize the effect of X-ray absorption by the samples, the wavelength of incident X-ray beam was set to 0.5 Å using a silicon monochromator, which was calibrated with NIST standard reference material CeO_2 as an external standard reference. Structural parameters were refined by Rietveld method with the program RIETAN-FP[48] and the program Z-Rietveld (version 1.1.3 for Windows).[49] Schematic illustrations of the crystal structures of the sample were drawn using the program VESTA.[50] Structural changes during an initial charging and discharging processes were examined for P2 type $Na_{2/3}[Ni_{1/3}Mn_{2/3}]O_2$, $Na_{2/3}[Ni_{1/3}Mn_{1/3}Ti_{1/6}]O_2$, and $Na_{2/3}[Ni_{1/4}Mn_{1/2}Ti_{1/6}Zn_{1/12}]O_2$ by an operando XRD technique using a battery-cell attachment (Rigaku Corporation)[51] and the data were collected by an X-ray diffractometer (MultiFlex, Rigaku Corporation) equipped with a high-speed position sensitive detector (D/teX Ultra, Rigaku Corporation) and non-monochromatized but Ni-filtered Cu Kα radiation as an X-ray source.

Particle morphology of the samples was observed by using a scanning electron microscope (SEM, JCM-6000, JEOL Ltd.) equipped with an energy-dispersive X-ray spectrometer. The outermost surface structure and morphology of the samples were observed with the JEM-2100F transmission electron microscope (TEM, JEOL Ltd.) at an accelerating voltage of 200 kV. Selected area electron diffraction (SAED) patterns of the samples were also collected with the microscope. The composition of the non-washed and washed $Na_{2/3}[Ni_{1/4}Mn_{1/2}Ti_{1/6}Zn_{1/12}]O_2$ samples was confirmed by inductively coupled plasma atomic emission spectrometry (ICP-AES) using SPS3500 (Hitachi High-Tech Corporation).

Electrochemical Characterization: Positive electrodes were prepared by following procedures. A slurry with a mixture of 80 wt% $Na_{2/3}[Ni_{1/3-x}Mn_{2/3-y}Me_xTi_y]O_2$, 10 wt% acetylene black (AB, Strem Chemicals, Inc.) and 10 wt% poly(vinylidene fluoride) (PVdF, Polysciences, Inc.) with *N*-methylpyrrolidone (Kanto Chemical Co., Ltd.) as a solvent was prepared, pasted on an aluminum foil and then dried at 80 °C under vacuum. Single-side-coated electrodes were punched into 10 or 15 mm disks in diameter for R2032 type coin cells with an Al-clad type of stainless-steel cap for the positive electrode side (Hohsen Corp.). The active material loading was ≈2.5 mg cm^{-2}. The separator used was glass fiber filter (GB-100R, ADVANTEC, Co.), the electrolyte solution was 1.0 mol dm^{-3} $NaPF_6$ dissolved in PC (Kishida Chemical Co., Ltd.), and the negative electrode was sodium metal (purity > 99%, Kanto Chemical Co., Ltd.). The electrode preparation and fabrication of the coin cells were carried out in an Ar-filled glove box. Galvanostatic charge–discharge tests were conducted with a charge/discharge measurement system (TOSCAT-3100, TOYO System Co., Ltd.) in the voltage range of 2.5–4.5 V at C/20 (≈13.0 mA g^{-1}) at 25 °C.

Hard X-ray Absorption Spectroscopy: Hard X-ray absorption spectroscopy (XAS) was performed at beam line BL-12C in the Photon Factory,

High Energy Accelerator Research Organization (KEK), Japan. The spectra were collected with a silicon monochromator in a transmission mode. The intensity of incident and transmitted X-ray was measured using ionization chambers at room temperature. The energy was calibrated by setting the first inflection point in the spectrum of a Cu foil to 8979 eV. Na-extracted electrode samples were electrochemically prepared in the coin cells. The positive electrodes were taken out from the coin cells, rinsed with PC and DEC and then dried at room temperature in an Ar-filled glovebox. The several electrodes with Al-foil current collectors were stacked and sealed in an oxygen- and moisture-barrier polymer film in the Ar-filled glovebox. The Ni K-edge spectrum of $LaNiO_3$ (99.9%, Kojundo Chemical Laboratory Co., Ltd.) mixed with BN (99%, Kanto Chemical Co., Ltd.) powder was measured as a standard reference. Absorption spectroscopy data were normalized and treated using the ATHENA program on the Demeter software package.[52] Fourier transformation of the $\chi(k)k^3$–k plots, where χ and k are oscillatory components of the normalized absorption and angular wavenumber, respectively, was performed using the ATHENA program.

Supporting Information

Supporting Information is available from the Wiley Online Library or from the author.

Acknowledgements

This study was in part supported by the Japan Science and Technology Agency (JST) through the Adaptable and Seamless Technology Transfer Program through Target driven R&D (A-STEP), Project No. AS2614056L through the CONCERT-Japan program of the Strategic International Research Cooperative Program (SICORP), Grant No. JPMJSC17C1, through the program of Core Research for Evolutional Science and Technology (CREST), Grant No. JPMJCR21O6, and by the Element Strategy Initiative of the Ministry of Education Culture, Sports, Science and Technology, Japan (MEXT), Grant Number JPMXP0112101003. The synchrotron X-ray diffraction experiments were performed at the BL02B2 of SPring-8 with the approval of JASRI (Proposal No. 2017B1312). The neutron-scattering experiments were approved by the Neutron Science Proposal Review Committee of J-PARC/MLF (Proposal No. 2014PM0005). The synchrotron X-ray absorption work was done under the approval of the Photon Factory Program Advisory Committee (Proposal No. 2014G055 and 2018G673). This research was supported in part financially by BASF SE. The authors thank Ms. Sayuri Fukuyama, Dr. Zhen-Ji Han, and Dr. Hitoshi Fukumitsu (BASF Japan Ltd.) for their advice and fruitful discussion. The authors are grateful to Dr. Toshinari Ichihashi and Prof. Yasushi Idemoto in the Tokyo University of Science for TEM measurements.

Conflict of Interest

The authors declare no conflict of interest.

Data Availability Statement

The data that support the findings of this study are available from the corresponding author upon reasonable request.

Keywords

cathode materials, intercalation, layered oxides, sodium batteries, structural analysis, substitution, superstructure

Received: January 23, 2023
Revised: April 6, 2023
Published online: May 13, 2023

[1] C. Delmas, *Adv. Energy Mater.* **2018**, *8*, 1703137.
[2] N. Yabuuchi, K. Kubota, M. Dahbi, S. Komaba, *Chem. Rev.* **2014**, *114*, 11636.
[3] C. Vaalma, D. Buchholz, M. Weil, S. Passerini, *Nat. Rev. Mater.* **2018**, *3*, 18013.
[4] S. Komaba, W. Murata, T. Ishikawa, N. Yabuuchi, T. Ozeki, T. Nakayama, A. Ogata, K. Gotoh, K. Fujiwara, *Adv. Funct. Mater.* **2011**, *21*, 3859.
[5] A. Kamiyama, K. Kubota, D. Igarashi, Y. Youn, Y. Tateyama, H. Ando, K. Gotoh, S. Komaba, *Angew. Chem., Int. Ed.* **2021**, *60*, 5114.
[6] Z. H. Lu, J. R. Dahn, *Chem. Mater.* **2001**, *13*, 1252.
[7] Z. H. Lu, J. R. Dahn, *J. Electrochem. Soc.* **2001**, *148*, A1225.
[8] D. H. Lee, J. Xu, Y. S. Meng, *Phys. Chem. Chem. Phys.* **2013**, *15*, 3304.
[9] H. Yoshida, N. Yabuuchi, K. Kubota, I. Ikeuchi, A. Garsuch, M. Schulz-Dobrick, S. Komaba, *Chem. Commun.* **2014**, *50*, 3677.
[10] X. H. Wu, G. L. Xu, G. M. Zhong, Z. L. Gong, M. J. McDonald, S. Y. Zheng, R. Q. Fu, Z. H. Chen, K. Amine, Y. Yang, *ACS Appl. Mater. Interfaces* **2016**, *8*, 22227.
[11] K. Wang, H. Wan, P. F. Yan, X. Chen, J. J. Fu, Z. X. Liu, H. Q. Deng, F. Gao, M. L. Sui, *Adv. Mater.* **2019**, *31*, 1904816.
[12] Q. J. Mao, Y. Yu, J. K. Wang, L. R. Zheng, Z. Y. Wang, Y. S. Qiu, Y. M. Hao, X. F. Liu, *J. Mater. Chem. A* **2021**, *9*, 10803.
[13] L. Q. Mu, Q. P. Hou, Z. Z. Yang, Y. Zhang, M. M. Rahman, D. J. Kautz, E. Sun, X. W. Du, Y. G. Du, D. Nordlund, F. Lin, *J. Electrochem. Soc.* **2019**, *166*, A251.
[14] Y. Y. Huang, Z. C. Yan, W. Luo, Z. W. Hu, G. X. Liu, L. L. Zhang, X. L. Yang, M. Y. Ou, W. J. Liu, L. Q. Huang, H. J. Lin, C. T. Chen, J. H. Luo, S. Li, J. T. Han, S. L. Chou, Y. H. Huang, *Energy Storage Mater.* **2020**, *29*, 182.
[15] K. Kubota, S. Kumakura, Y. Yoda, K. Kuroki, S. Komaba, *Adv. Energy Mater.* **2018**, *8*, 1703415.
[16] Y. S. Wang, R. J. Xiao, Y. S. Hu, M. Avdeev, L. Q. Chen, *Nat. Commun.* **2015**, *6*, 6954.
[17] P. F. Wang, H. R. Yao, X. Y. Liu, Y. X. Yin, J. N. Zhang, Y. R. Wen, X. Q. Yu, L. Gu, Y. G. Guo, *Sci. Adv.* **2018**, *4*, eaar6018.
[18] A. Gutierrez, W. M. Dose, O. Borkiewicz, F. M. Guo, M. Avdeev, S. Kim, T. T. Fister, Y. Ren, J. Bareno, C. S. Johnson, *J. Phys. Chem. C* **2018**, *122*, 23251.
[19] A. J. Williams, J. P. Attfield, M. L. Foo, L. Viciu, R. J. Cava, *Phys. Rev. B: Condens. Matter Mater. Phys.* **2006**, *73*, 134401.
[20] T. A. Platova, I. R. Mukhamedshin, H. Alloul, A. V. Dooglav, G. Collin, *Phys. Rev. B: Condens. Matter Mater. Phys.* **2009**, *80*, 224106.
[21] M. Guignard, C. Didier, J. Darriet, P. Bordet, E. Elkaim, C. Delmas, *Nat. Mater.* **2013**, *12*, 74.
[22] X. Li, X. H. Ma, D. Su, L. Liu, R. Chisnell, S. P. Ong, H. L. Chen, A. Toumar, J. C. Idrobo, Y. C. Lei, J. M. Bai, F. Wang, J. W. Lynn, Y. S. Lee, G. Ceder, *Nat. Mater.* **2014**, *13*, 586.
[23] K. Kubota, M. Miyazaki, E. J. Kim, H. Yoshida, P. Barpanda, S. Komaba, *J. Mater. Chem. A* **2021**, *9*, 26810.
[24] C. L. Zhao, F. X. Ding, Y. X. Lu, L. Q. Chen, Y. S. Hu, *Angew. Chem., Int. Ed.* **2020**, *59*, 264.
[25] F. X. Ding, C. L. Zhao, D. D. Xiao, X. H. Rong, H. B. Wang, Y. Q. Li, Y. Yang, Y. X. Lu, Y. S. Hu, *J. Am. Chem. Soc.* **2022**, *144*, 8286.
[26] L. B. Yao, P. C. Zou, C. Y. Wang, J. H. Jiang, L. Ma, S. Tan, K. A. Beyer, F. Xu, E. Y. Hu, H. L. L. Xin, *Adv. Energy Mater.* **2022**, *12*, 2201989.
[27] C. Delmas, J. J. Braconnier, A. Maazaz, P. Hagenmuller, *Rev. Chim. Miner.* **1982**, *19*, 343.
[28] S. C. Abrahams, J. L. Bernstein, *Acta Crystallogr., Sect. B: Struct. Crystallogr. Cryst. Chem.* **1969**, *B25*, 1233.
[29] N. Yabuuchi, R. Hara, M. Kajiyama, K. Kubota, T. Ishigaki, A. Hoshikawa, S. Komaba, *Adv. Energy Mater.* **2014**, *4*, 1301453.
[30] J. M. Paulsen, R. A. Donaberger, J. R. Dahn, *Chem. Mater.* **2000**, *12*, 2257.

[31] Z. H. Lu, R. A. Donaberger, J. R. Dahn, *Chem. Mater.* **2000**, *12*, 3583.
[32] R. Berthelot, D. Carlier, C. Delmas, *Nat. Mater.* **2011**, *10*, 74.
[33] V. F. Sears, *J. Neutron Res.* **1992**, *3*, 26.
[34] D. Igarashi, Y. Miyazaki, T. Kajitani, K. Yubuta, *Phys. Rev. B: Condens. Matter Mater. Phys.* **2008**, *78*, 184112.
[35] R. Shannon, *Acta Crystallogr* **1976**, *32*, 751.
[36] Y. Zhang, M. M. Wu, W. Teng, J. W. Ma, R. Y. Zhang, Y. H. Huang, *ACS Appl. Mater. Interfaces* **2020**, *12*, 15220.
[37] K. Kubota, S. Komaba, *J. Electrochem. Soc.* **2015**, *162*, A2538.
[38] N. Yabuuchi, M. Kajiyama, J. Iwatate, H. Nishikawa, S. Hitomi, R. Okuyama, R. Usui, Y. Yamada, S. Komaba, *Nat. Mater.* **2012**, *11*, 512.
[39] K. Kubota, Y. Yoda, S. Komaba, *J. Electrochem. Soc.* **2017**, *164*, A2368.
[40] J. W. Somerville, A. Sobkowiak, N. Tapia-Ruiz, J. Billaud, J. G. Lozano, R. A. House, L. C. Gallington, T. Ericsson, L. Haggstrom, M. R. Roberts, U. Maitra, P. G. Bruce, *Energy Environ. Sci.* **2019**, *12*, 2223.
[41] W. H. Zuo, F. C. Ren, Q. H. Li, X. H. Wu, F. Fang, X. Q. Yu, H. Li, Y. Yang, *Nano Energy* **2020**, *78*, 105285.
[42] K. H. Dai, J. Mao, Z. Q. Zhuo, Y. Feng, W. F. Mao, G. Ai, F. Pan, Y. D. Chuang, G. Liu, W. L. Yang, *Nano Energy* **2020**, *74*, 104831.
[43] K. Wang, P. F. Yan, M. L. Sui, *Nano Energy* **2018**, *54*, 148.
[44] Y. Yoda, K. Kubota, H. Isozumi, T. Horiba, S. Komaba, *ACS Appl. Mater. Interfaces* **2018**, *10*, 10986.
[45] S. Guo, Q. Li, P. Liu, M. Chen, H. Zhou, *Nat. Commun.* **2017**, *8*, 135.
[46] F. Zhang, J. Liao, L. Xu, W. Wu, X. Wu, *ACS Appl. Mater. Interfaces* **2021**, *13*, 40695.
[47] S. Kawaguchi, M. Takemoto, K. Osaka, E. Nishibori, C. Moriyoshi, Y. Kubota, Y. Kuroiwa, K. Sugimoto, *Rev. Sci. Instrum.* **2017**, *88*, 085111.
[48] F. Izumi, K. Momma, *Solid State Phenom.* **2007**, *130*, 15.
[49] R. Oishi, M. Yonemura, Y. Nishimaki, S. Torii, A. Hoshikawa, T. Ishigaki, T. Morishima, K. Mori, T. Kamiyama, *Nucl. Instrum. Methods Phys. Res., Sect. A* **2009**, *600*, 94.
[50] K. Momma, F. Izumi, *J. Appl. Crystallogr.* **2011**, *44*, 1272.
[51] *Rigaku J.* **2011**, *27*, 32.
[52] B. Ravel, M. Newville, *J. Synchrotron Radiat.* **2005**, *12*, 537.